ACS Sustainable Chemistry & Engineering

Research Article

Cite This: ACS Sustainable Chem. Eng. 2018, 6, 5105−5114

pubs.acs.org/journal/ascecg

Total Water Splitting Catalyzed by Co@Ir Core−Shell Nanoparticles Encapsulated in Nitrogen-Doped Porous Carbon Derived from Metal−Organic Frameworks

Dongliang Li,[†] Zhuo Zong,[†] Zhenghua Tang,*[,‡,§] Zhen Liu,[∥] Shaowei Chen,[‡,⊥] Yong Tian,[†] and Xiufang Wang*[,†]

[†]School of Pharmacy, Guangdong Pharmaceutical University, 280 Waihuandong Road, Guangzhou Higher Education Mega Centre, Guangzhou, 510006, P. R. China

[‡]Guangzhou Key Laboratory for Surface Chemistry of Energy Materials and New Energy Research Institute, School of Environment and Energy, South China University of Technology, Guangzhou Higher Education Mega Centre, Guangzhou, 510006, P. R. China

[§]Guangdong Provincial Key Laboratory of Atmospheric Environment and Pollution Control, Guangdong Provincial Engineering and Technology Research Center for Environmental Risk Prevention and Emergency Disposal, South China University of Technology, Guangzhou Higher Education Mega Centre, Guangzhou, 510006, P. R. China

[∥]Department of Physics & Engineering, Frostburg State University, Frostburg, Maryland 21532-2303, United States

[⊥]Department of Chemistry and Biochemistry, University of California, 1156 High Street, Santa Cruz, California 95064, United States

Supporting Information

ABSTRACT: Developing bifunctional electrocatalysts for oxygen evolution reaction (OER) and hydrogen evolution reaction (HER) toward overall water splitting with high efficiency and robust durability is highly desirable but very challenging. Herein, we report a highly efficient and robust bifunctional electrocatalyst for overall water splitting based on Co@Ir core−shell nanoparticles encapsulated in nitrogen-doped porous carbon derived from metal−organic frameworks. The series of Co@Ir/NC-*x* samples were prepared through a galvanic replacement of $IrCl_3$ with Co/NC, which was obtained by calcination of zeolitic imidazolate framework 67 (ZIF-67). In the electrocatalytic characterizations toward OER and HER, Co@Ir/NC-10% exhibited the best performance among the series, with an overpotential of 280 mV at a current density of 10 mA cm^{-2} for OER, superior to the benchmark IrO_2 catalyst, and an overpotential of −121 mV at a current density of 10 mA cm^{-2} for HER in 1 M KOH. Moreover, Co@Ir/NC-10% also demonstrated markedly higher long-term stability than IrO_2 for OER and superior long-term durability than Pt/C for HER. Finally, the overall water splitting catalyzed by the series of composites was explored and visually observed.

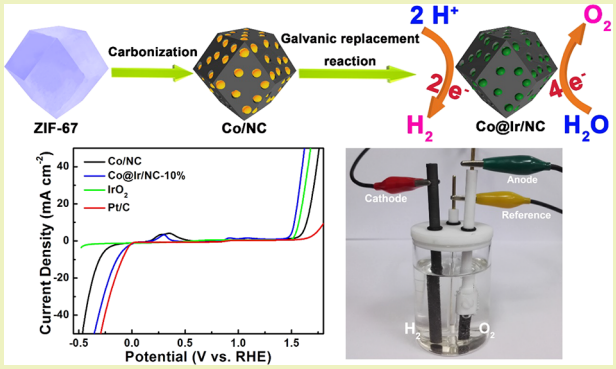

KEYWORDS: *Co@Ir core−shell nanoparticles, Nitrogen-doped porous carbon, Oxygen evolution reaction, Hydrogen evolution reaction, Overall water splitting*

INTRODUCTION

With the increasing concerns about rapid fossil fuel depletion and severe environmental pollution, it is essential to develop renewable and sustainable energy sources.[1−6] Due to its high energy storage density and negligible pollution nature, hydrogen has been widely considered as the most ideal energy carrier as an alternative to fuels.[7−9] Electrochemical overall water splitting is the most promising technology for large-scale hydrogen production.[10−12] The overall water splitting process includes oxygen evolution reaction (OER) and hydrogen evolution reaction (HER), unfortunately, both OER and HER need highly active electrocatalysts to reduce their large overpotentials.[13−15] Moreover, to realize the continual water splitting for real applications, the reaction must be operated in the same electrolyte (e.g., in alkaline solution). Therefore, developing a highly efficient electrocatalyst for overall water splitting in the same electrolyte, as well as lowering the costs, is quite appealing for large-scale hydrogen production.

Compared with HER, OER is the half reaction which determines the water splitting efficiency due to its intrinsically quite sluggish four-electron transfer process. It is well-known that iridium (Ir) has been regarded as the state-of-art

Received: December 18, 2017
Revised: February 6, 2018
Published: March 1, 2018

DOI: 10.1021/acssuschemeng.7b04777
ACS Sustainable Chem. Eng. 2018, 6, 5105−5114

electrocatalyst for OER in alkaline solution.[16−20] Unfortunately, its abundance in the Earth's crust is even lower than that of platinum; hence, it suffers from scarcity and high cost. Alloying Ir with a transition metal is generally believed as a viable and effective strategy which can not only reduce the usage of Ir but also enhance its catalytic properties by modifying the d-band structure of the IrO_x surface.[21,22] For instance, Hu and Chen et al. discovered that the Co-rich CoIr binary oxide is about two times more active and much more durable during oxygen evolution under a constant potential of 1.6 V.[23] By using Cu nanoparticles as a template, single-crystalline Cu−Ir polyhedral nanocages were prepared by the Zou group,[24] and the $Cu_{1.1}Ir$ nanocages exhibited excellent catalytic performance with a overpotential of −286 mV at a current density of 10 mA cm^{-2}, and a small Tafel slope of 43.8 mV dec^{-1} in 0.05 M H_2SO_4. Recently, Pi et al. developed a highly efficient overall water splitting route by utilizing ultrasmall, monodispersed IrM (M = Fe, Co, Ni) clusters through a wet-chemical strategy.[25] In addition, IrCu nanoframes,[26] IrNi oxide,[27] as well as organometallic Ir complexes[28,29] have been documented to catalyze OER or overall water splitting as well.

Although significant progresses have been made in the past decade, several important issues still remain in the Ir-based electrocatalysts. First of all, most of these Ir based catalysts possess an alloyed structure, and the inner Ir atoms are not fully exposed and utilized. A core−shell structure with Ir as the shell would maximally expose the electrochemical catalytically active sites and hence is intriguing and desirable. Second, with either Ir based alloys or core−shell structure alone directly for overall water splitting, the cost is still very high and hence not favorable for large-scale production. The introduction of a carbon support such as nitrogen-doped porous carbon could significantly mitigate this issue. Note that, heteroatom doped porous carbon has been extensively and intensively employed in energy storage and conversion, thanks to its easy accessibility, excellent conductivity, and abundant active sites.[30−32]

Herein, we report a highly efficient overall water splitting electrocatalyst with Co@Ir core−shell nanoparticles that are encapsulated in nitrogen-doped porous carbon derived from metal−organic frameworks. The Co@Ir core−shell structure was revealed and confirmed by high-resolution transmission electron microscopy (HR-TEM), high-angle annular dark-field scanning tunneling electron microscopy (HAADF-STEM), and energy dispersive X-ray spectroscopy (EDX). The crystal structure and surface chemical states of the composites were examined by X-ray diffraction (XRD) and X-ray photoelectron spectroscopy (XPS), respectively. In the electrocatalytic characterizations toward OER and HER, Co@Ir/NC-10% exhibited the best performance among the series, with an overpotential of 280 mV at a current density of 10 mA cm^{-2} for OER, superior to the benchmark IrO_2 catalyst, and an overpotential of −121 mV at a current density of 10 mA cm^{-2} for HER in 1 M KOH. Moreover, Co@Ir/NC-10% also demonstrated markedly higher long-term stability than IrO_2 for OER and superior long-term durability than Pt/C for HER. Finally, the overall water splitting catalyzed by the series of composites was explored and visually observed.

EXPERIMENTAL SECTION

Materials. Cobalt nitrate hexahydrate ($Co(NO_3)_2·6H_2O$) and methanol were obtained from Fuchen Chemical Reagents (Tianjin, China). 2-Methylimidazole (MeIM) and iridium chloride hydrate ($IrCl_3·3H_2O$) and iridium oxide (IrO_2) were purchased from Energy Chemicals (Shanghai, China). Commercial 20 wt % Pt/C was acquired from Alfa Aesar. Distilled water with a resistivity of 18.3 MΩ·cm^{-1} was used in this work. All chemicals were used as received without further purification.

Synthesis of ZIF-67 Nanocrystals. ZIF-67 nanocrystals were synthesized according to a procedure reported previously.[33] In a typical preparation, 24 mmol of $Co(NO_3)_2·6H_2O$ was first dissolved in 240 mL of methanol and 96 mmol 2-methylimidazole was dissolved in 80 mL of methanol separately. Then the two solutions were mixed, stirred for 10 min, and incubated at room temperature for 24 h. Dark blue precipitates formed and were separated by centrifugation, washed with methanol several times, and then dried at 50 °C for 12 h in a vacuum oven.

Preparation of Co/NC. The ZIF-67 nanocrystals prepared above were pyrolyzed at controlled temperatures by the following procedure. Typically, 2 g of ZIF-67 nanocrystals were placed in a tube furnace and then heated to 900 °C for 3 h under an Ar atmosphere. After that, the furnace was cooled down to room temperature naturally. The obtained black powder was referred to as Co/NC.

Preparation of Co@Ir/NC-*x*. The synthesis of Co@Ir/NC-*x* (in which *x* represents the mass percentage of Ir in the sample) was conducted by following a modified procedure reported previously.[34] For the synthesis of Co@Ir/NC-5%, 50 mg of Co/NC prepared above was dispersed in 5 mL of deionized water and stirred for 15 min. Then, 4.38 mg of $IrCl_3·3H_2O$ dissolved in 2 mL of deionized water was injected into the above solution dropwise and stirred at 1000 rpm for 24 h at room temperature. After that, the suspension was centrifuged, while the black solids were collected and washed with water and methanol several times. The final product was dried under vacuum at 50 °C for 12 h. Co@Ir/NC-10% and Co@Ir/NC-15% were prepared in a similar manner in which the mass of Co/NC was unchanged while the mass of $IrCl_3·3H_2O$ was altered correspondingly.

Characterizations. The morphologies and structures were characterized by field-emission scanning electron microscopy (SEM, Hitachi S-4800) and transmission electron microscopy (TEM, Tecnai G2 F30). X-ray diffraction (XRD) patterns in the Bragg's angle (2θ) range of 5 to 90° were acquired using a Bruker D8 diffractometer with Cu Kα radiation (λ = 0.1541 nm). X-ray photoelectron spectroscopy (XPS) was performed by using an Escalab 250 photoelectron spectrometer (Thermo Fisher Scientific, USA). Brunauer−Emment−Teller (BET) surface areas and pore size measurements were performed with N_2 adsorption/adsorption isotherms at 77 K on a Quantachrome Autosorb-iQ2 instrument. Inductively coupled plasma mass spectrometric (ICP-MS) analysis was conducted with a PerkinElmer Nexion 300 instrument.

Electrochemical Measurements. Electrochemical measurements were conducted with a CHI 750E electrochemical workstation (CH Instruments Inc.) at room temperature. OER and water splitting tests were performed in 1 M KOH aqueous solution. A rotating ring disk electrode (RRDE) (diameter 5.0 mm) was employed as the working electrode and was cleaned by mechanical polishing with aqueous slurries of 0.3 μm alumina powders on a polishing microcloth. A platinum wire and a Ag/AgCl electrode ($E_{Ag/AgCl} = E_{RHE} + 0.966$ V) were used as the counter electrode and reference electrode, respectively. Five mg of the catalysts were first dispersed in 1 mL ethanol with 20 μL Nafion (5 wt %, Aldrich) to make a catalyst ink. The catalyst ink (10 μL) was then added dropwise onto the glassy carbon disk and dried at room temperature, and the catalyst loading was calculated to be 0.202 mg cm^{-2} for all samples. The RRDE with a gold ring was employed in LSV measurements, and the measurements were conducted in an N_2-saturated 1 M KOH solution at the rotation of 1600 rpm in the potential range of 0−1.0 V with a scan rate of 10 mV s^{-1}. For HER test, it was performed in both 0.5 M H_2SO_4 and 1 M KOH aqueous solution. A carbon rod (diameter 3.0 mm) and Hg/Hg_2Cl_2 were used as the counter and the reference electrode, respectively. The catalyst loading was approximately 0.357 mg cm^{-2}. LSV measurements were conducted in the potential range of −0.8 to 0 V (in 0.5 M H_2SO_4) and −1.5 to −0.7 V (in 1 M KOH) with a scan rate of 10 mV s^{-1}. Cyclic voltammetric (CV) measurements were

DOI: 10.1021/acssuschemeng.7b04777
ACS Sustainable Chem. Eng. 2018, 6, 5105−5114

Scheme 1. Schematics of the Preparation of the Series of Co@Ir/NC Composites

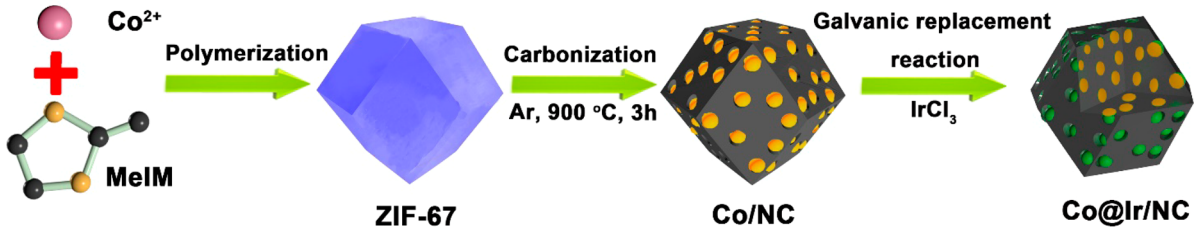

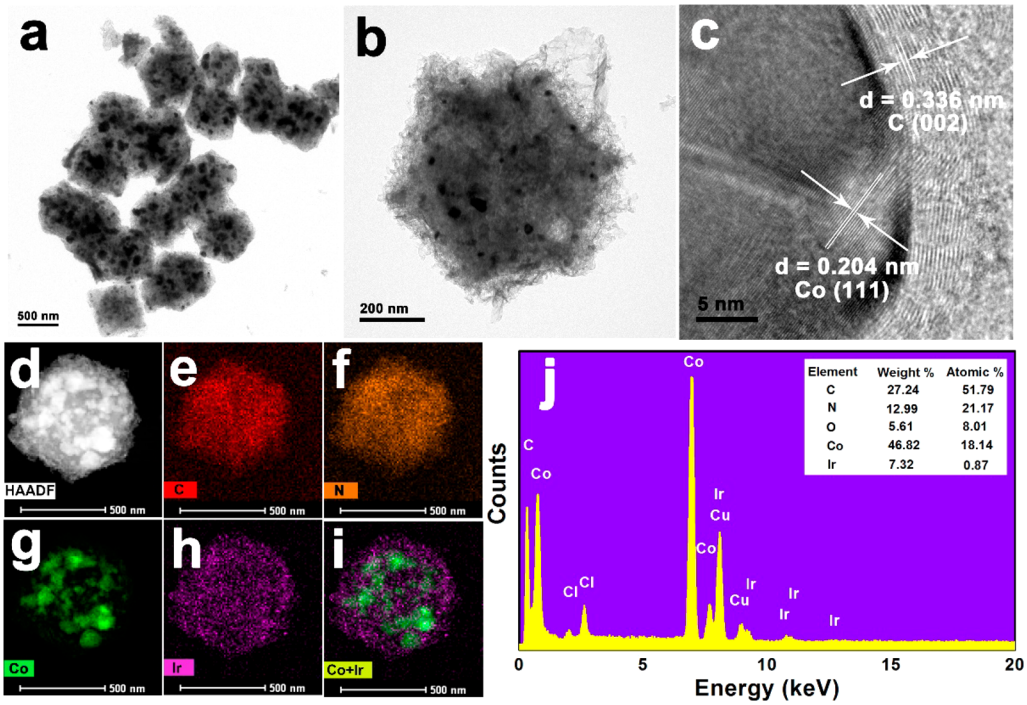

Figure 1. (a) Representative TEM image and (b, c) HR-TEM images of Co@Ir/NC-10%. (d) Typical HAADF-STEM image of Co@Ir/NC-10% at low magnification and corresponding EDS elemental mapping of (e) C, (f) N, (g) Co, (h) Ir, and (i) Co+Ir. (j) EDX spectrum of the Co@Ir/NC-10% particles (inset) Elemental content of C, N, O, Co, and Ir in Co@Ir/NC-10% sample.

conducted in 0.05 M H_2SO_4 solution with a scan rate of 50 mV s^{-1}. Finally, chronoamperometric responses for OER was conducted in 1 M KOH solution at +0.55 V for 30 000 s, while accelerated durability tests (ADT) for HER were performed by cycling the catalyst over the potential range of −0.3 to 0 V for 3000 cycles with a scan rate of 50 mV s^{-1} in 0.5 M H_2SO_4 solution.

RESULTS AND DISCUSSION

The Co@Ir/NC composites were first prepared by following the schematics illustrated in Scheme 1.[34,35] Briefly, the polymerization between Co^{2+} ions and MeIM led to the formation of ZIF-67, which underwent carbonization at 900 °C under Ar atmosphere for 3 h to form Co/NC. The galvanic replacement reaction between $IrCl_3$ and Co/NC yielded the series of Co@Ir/NC-*x* samples eventually. The typical SEM images of ZIF-67, Co/NC, and the Co@Ir/NC-*x* series can be found in Figure S1. One can see that, ZIF-67 displayed a well-defined polyhedral shape with the size ranging from approximately 840 to 1100 nm, while such a polyhedral morphological skeleton can still be clearly recognized in Co/NC and the Co@Ir/NC-*x* samples. Figure S2 depicts the nitrogen adsorption and desorption isotherm and corresponding pore size distribution of ZIF-67, Co/NC, and the Co@Ir/NC-*x* series. It can be noted that ZIF-67 showed a type I isotherm and the calculated BET surface area was 1963.74 m^2 g^{-1}, implying that mostly micropores were formed. Co/NC exhibited isotherms of both type I and IV, corresponding to the formation of micropores and mesopores, respectively. Interestingly, when forming the Co@Ir/NC composite, with the rapid diminishing of micropores, the mesopores dominated the structure. The BET surface area of Co/NC, Co@Ir/NC-5%, Co@Ir/NC-10%, and Co@Ir/NC-15% was calculated as 239.48, 135.61, 108.45, and 105.79 m^2 g^{-1}, respectively. As a note, the well-defined mesopores have been documented to enhance the mass transport of reaction intermediates thus probably favorable for the electrochemical reaction kinetics.[34,36]

The shape and surface microstructures of the series samples were then observed by transmission electron microscopy (TEM) and high-resolution transmission electron microscopy (HR-TEM). From the typical TEM image in Figure 1a and HR-TEM image in Figure 1b, the Co@Ir/NC-10% sample showed a dodecahedron-like morphology with a diameter of approximately 600−800 nm. The carbon layer can be clearly identified from the HR-TEM image of a single particle (Figure 1c), and the lattice space of ∼0.336 nm is ascribed to the C (002) plane. In addition, the lattice space in the center of ∼0.204 nm is attributed to the Co (111) plane. Then high-angle annular dark-field scanning tunneling electron micros-

DOI: 10.1021/acssuschemeng.7b04777
ACS Sustainable Chem. Eng. 2018, 6, 5105−5114

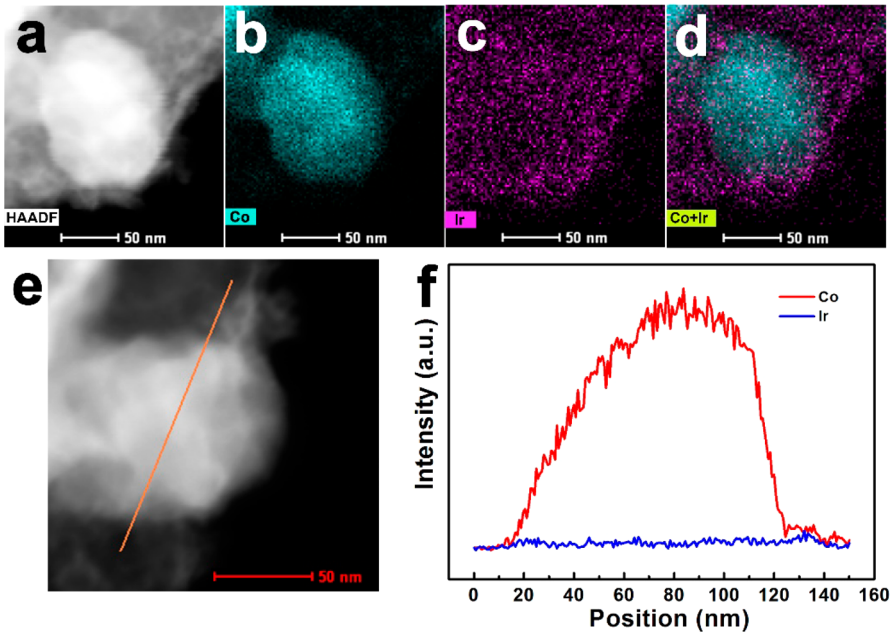

Figure 2. (a) Typical HAADF-STEM image of a Co@Ir particle in Co@Ir/NC-10% sample, and corresponding EDS elemental mapping of (b) Co, (c) Ir, and (d) Co+Ir at high magnification. (e) HAADF-STEM image and cross-sectional compositional line-scanning profile (f) of a Co@Ir particle.

copy (HAADF-STEM) and energy dispersive X-ray spectroscopy (EDX) were conducted to probe the elemental mapping of the composite. From the lower magnification HAADF-STEM images shown in Figure 1d–i, the cobalt, iridium, carbon, and nitrogen elements are uniformly distributed. Particularly, the iridium elements are surrounding the cobalt elements, indicating the formation of a core–shell structure. The EDX spectra of the Co@Ir/NC-10% (Figure 1j) further attest the coexistence of all the elements, where the Ir weight percentage was only 7.32%, lower than the initial loading percentage (10%). It is worth noting that, for all the samples, the actual Ir weight percentage determined from inductively coupled plasma mass spectrometry (ICP-MS) is lower than the initial loading values, as summarized in Table S1.

Such observation was further confirmed by the high-magnification HAADF-STEM images presented in Figure 2a–d, as high-density cobalt elements are located in the core where iridium elements are on every side all around the core. The extrapolated line-scanning profile (Figure 2f) from an individual particle (Figure 2e) shows that Ir was in a markedly lower concentration, somewhat enriched at the edges where Co exhibited a peak-shaped distribution, consistent with the formation of a Co-rich core and an Ir-rich shell. In addition, the representative HR-TEM images of Co/NC and the other samples in the Co@Ir/NC-*x* series can be found in Figure S3, and all samples exhibited similar structural feature as Co/NC.

The crystal structures of the Co@Ir/NC composites were next examined by XRD measurements. As illustrated in Figure 3a, similar diffraction features of a broad and weak peak from C (002) can be observed for the series of samples, indicating the existence of carbon layers. In addition, a series of Bragg reflections corresponding to the diffractions from Co (111), Co (200), and Co (220) (JCPDS card no. 15-0806) can be easily identified while no signal from Ir was detected, suggesting Ir atoms were in situ buried in nitrogen-doped porous carbon and were present in an extremely low amount, which is in good agreement with the value discussed above. Subsequently, the chemical states of the composites detected by X-ray photoelectron spectroscopy (XPS) are illustrated in Figure 3b–f. The appearance of the Co 3p, O 1s, C 1s, and Ir 4f peaks in the survey scan spectra (Figure 3b) of the Co@Ir/NC-10% sample confirmed the presence of C, O, Co, and Ir elements. The XPS survey scan spectra comparison of Co/NC, Co@Ir/NC-5%, Co@Ir/NC-10%, and Co@Ir/NC-15% can be found in Figure S4, and the Co@Ir/NC-*x* series displayed similar feature, with a slight variation of Ir signal. Figure 3c depicts the core-level spectra of the C 1s electrons. The bulky peak at ~284.8 eV can be deconvoluted into four distinct peaks (284.7 eV from carbon in C–C, 285.7 eV from carbon in C–N, 286.6 eV from carbon in C=N and 289.0 eV from carbon in C–C=O), indicating the presence of four distinct species.[37] Similarly, the peak from the N 1s electrons (Figure 3d) for the Co@Ir/NC-10% sample with a binding energy of approximately 400.8 eV, can also be deconvoluted into two defined species including pyridinic N (~398.3 eV) and graphitic N (~400.9 eV), which agree well with the previous reports.[35,38,39] The core-level spectra of the Co 2p electrons from Co@Ir/NC-10% and Co/NC are presented in Figure 3e. The binding energies at ~781.9 and ~780.0 eV can be attributed to the Co $2p_{3/2}$ electrons from Co@Ir/NC-10% and Co/NC, respectively. It can be noted that, the binding energy of the Co 2p electrons from Co@Ir/NC-10% is approximately 1.9 eV higher than that of Co/NC. This indicates that the electron transfer occurred from the Co core to the Ir shell. For the peak from Co $2p_{3/2}$ electrons, upon deconvolution, three pairs of peaks can be identified for both samples. For Co@Ir/NC-10%, the peaks centered at 781.8 eV probably arose from Co^{2+}, with a satellite peak at 786.5 eV, while the peak at 779.8 eV can be ascribed to metallic Co.[39−42] In addition, the high-resolution spectra of the Ir 4f electrons for Co@Ir/NC-10% and $IrCl_3$ are presented in Figure 3f. The binding energy at ~62.5 eV is attributed to the Ir $4f_{7/2}$ electrons from $IrCl_3$, while the Ir $4f_{7/2}$ electrons of Co@Ir/NC-10% exhibited a binding energy at ~62.3 eV, slightly lower than that of $IrCl_3$. Furthermore, the peak of the Ir $4f_{7/2}$ electrons from

DOI: 10.1021/acssuschemeng.7b04777
ACS Sustainable Chem. Eng. 2018, 6, 5105−5114

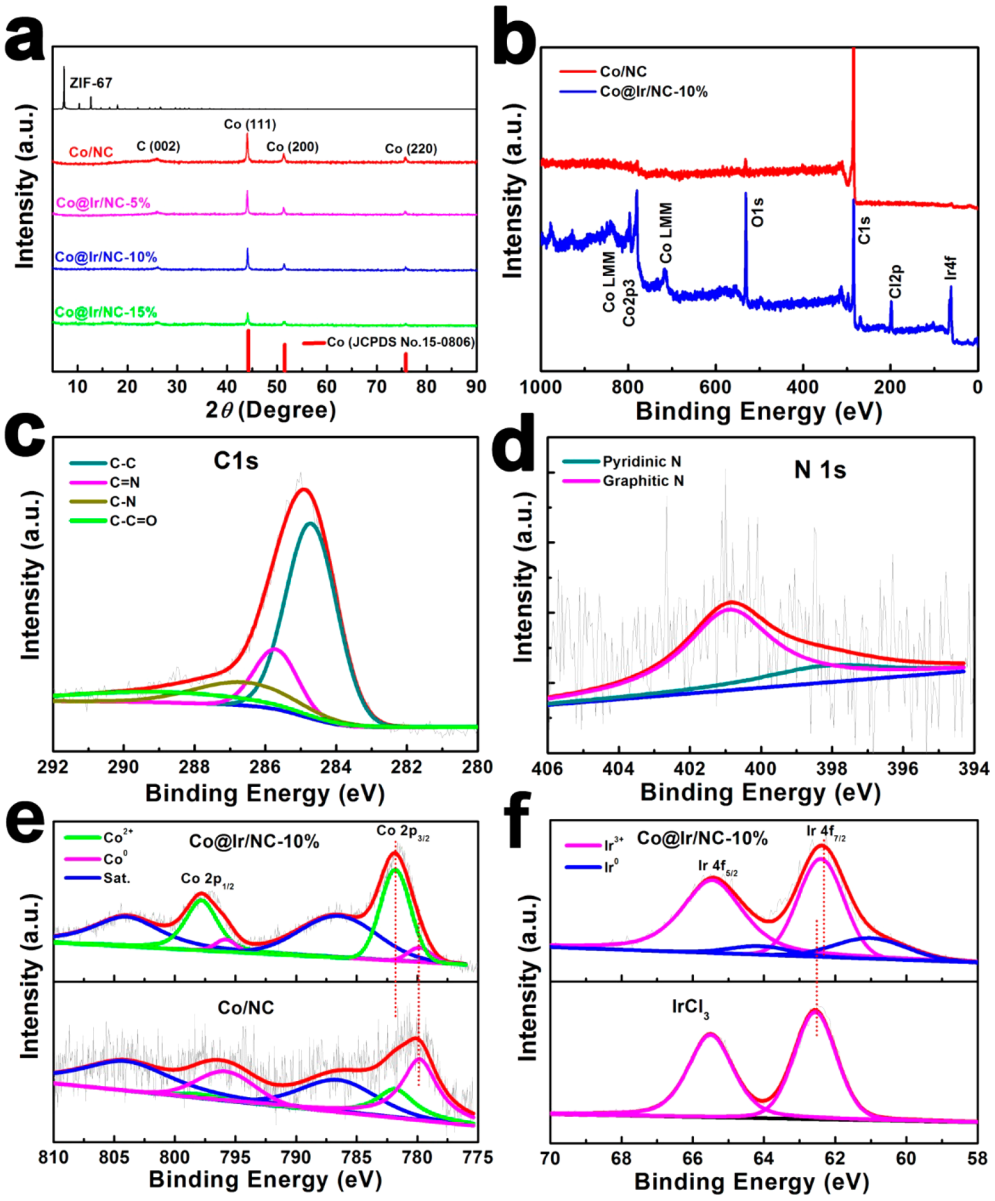

Figure 3. (a) XRD patterns, (b) XPS survey spectra, and core-level spectra of (c) C 1s, (d) N 1s, (e) Co 2p, and (f) Ir 4f electrons for the Co@Ir/NC-10% sample.

Co@Ir/NC can be deconvoluted into two peaks centered at ~62.4 and ~61.0 eV, corresponding metallic Ir and Ir^{3+}, respectively.[43−45]

The electrocatalytic performance of the series of samples toward OER was then explored in nitrogen-saturated 1 M KOH solution. As depicted in the linear sweep voltammograms (LSVs) in Figure 4a, to reach a current density of 10 mA cm^{-2}, the required potential was 1.70, 1.55, 1.51, 1.53, and 1.58 V for the sample of Co/NC, Co@Ir/NC-5%, Co@Ir/NC-10%, Co@Ir/NC-15%, and IrO_2, respectively. The OER and HER activity comparison of the series samples is compiled in Table S1. In the absence of Ir, Co/NC exhibited lower OER activity than the benchmark IrO_2 catalyst, however, superior activity than IrO_2 was obtained for the Co@Ir samples. Interestingly, with the increasing of Ir amount, the OER activity first increased then decreased, and the Co@Ir/NC-10% sample showed the best activity. The corresponding Tafel plots of the series of samples were then recorded and compared with IrO_2 in Figure 4b. The Co@Ir samples showed lower Tafel slope values than IrO_2, and the Co@Ir/NC-10% sample exhibited the lowest Tafel slope, further attest that superior activity than IrO_2 was achieved. The electrochemical impedance spectra of the series samples as well as IrO_2 can be found in Figure 4c. Co/NC shows a near-linear line in the wide frequency range, besides that, all the samples exhibited similar Nyquist pattern, with an up-sloping near-linear line in the high frequency range, followed by a semicircle bending toward the *x*-axis in the low frequency domain.[46] The series samples demonstrated lower charge transfer resistance than IrO_2. The Co@Ir/NC-10% sample possessed the lowest resistance, indicating the finest OER reaction kinetics among the series. Moreover, the long-term durability toward OER was evaluated by a chronoamperometric test at 1.62 V in 1 M KOH. As presented in Figure 4d, after continuous operation of ~12 h, the Co@Ir/NC-10% sample can retain 79.4% of its initial current, while in sharp contrast, IrO_2 only retained 44.2%. This indicates that remarkably higher durability of Co@Ir/NC-10% than that of IrO_2 was achieved.

DOI: 10.1021/acssuschemeng.7b04777
ACS Sustainable Chem. Eng. 2018, 6, 5105−5114

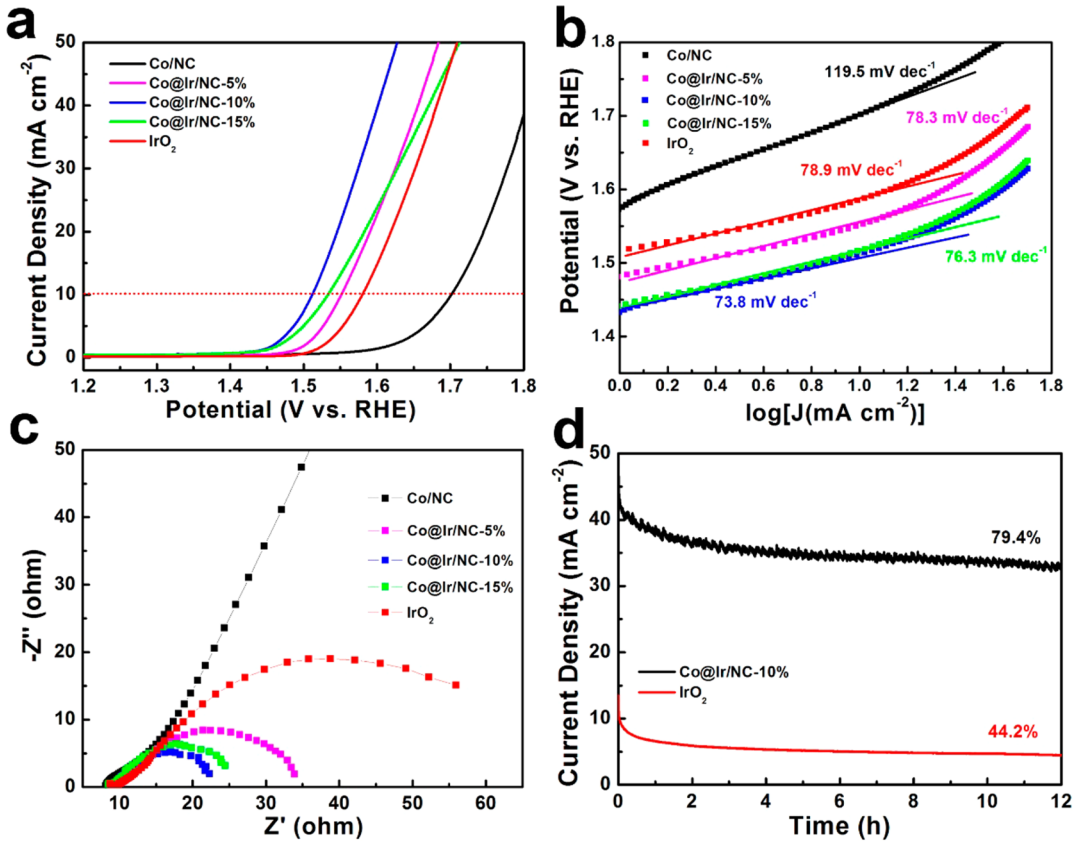

Figure 4. (a) LSV curves of Co/NC, Co@Ir/NC-5%, Co@Ir/NC-10%, Co@Ir/NC-15%, and IrO_2 in N_2-saturated 1 M KOH solution at the potential scan rate of 10 mV s^{-1}. (b) Tafel plots of different catalysts in OER derived from the OER polarization curves. (c) Electrochemical impedance spectra of different catalysts on the GCE electrode at +1.52 V versus RHE for OER conducted in 1 M KOH aqueous solution with an AC amplitude of 5 mV from the frequency range of 100 kHz to 0.01 Hz. (d) Long-term stability of Co@Ir/NC-10% and commercial IrO_2 catalyst.

Furthermore, the electrocatalytic activity toward HER of the series samples was assessed and compared with the state-of-art Pt/C catalyst in 1 M KOH. As a note, the HER performance was normally evaluated by comparing the required overpotential versus the reversible hydrogen electrode (RHE) to reach a current density of 10 mA cm^{-2}, which is the threshold current density expected for a 12.3% efficient solar water-splitting device.[7] The polarization curves are illustrated in Figure 5a. To afford a current density of 10 mA cm^{-2}, the required overpotential was −227, −198, −121, −147, and −41 mV for Co/NC, Co@Ir/NC-5%, Co@Ir/NC-10%, Co@Ir/NC-15%, and Pt/C, respectively. As expected, Pt/C possessed the best activity. Co/NC had the lowest activity and the HER activity actually first increased then decreased with the increasing of Ir, which is in good accordance of the trend observed in OER tests. Again, the Co@Ir/NC-10% sample possessed the best HER activity. The corresponding Tafel plots can be found in Figure 5b where the Tafel slope values were calculated and presented. Pt/C showed the lowest Tafel slope of 38 mV dec^{-1}, while Co/NC exhibited the highest value of 158.4 mV dec^{-1}. The Co@Ir/NC-10% sample had the lowest Tafel slope value among the series, which is close to that of Pt/C, suggesting a rapid HER rate and a Tafel−Volmer mechanism where the electrochemical desorption of H_2 is the rate-determining step in the HER process.[42,47] Subsequently, the electrochemical impedance spectroscopic investigation of the series of samples as well as Pt/C was conducted to further probe the electron transfer kinetics.[48] Figure 5c depicts the Nyquist plots acquired at −0.07 V for a GCE modified with the various catalyst samples. Pt/C exhibited the smallest resistance as expected, while Co/NC possessed the largest charge transfer resistance, as a near-linear line was observed. All the Co@Ir/NC-x samples exhibited a smaller semicircle than IrO_2, indicating a lower resistance, in good accordance with better activity than IrO_2 observed in HER test. Among the series, Co@Ir/NC-10% showed the lowest charge transfer resistance, as manifested by the smallest semicircle, consistent with the best HER performance. Durability is another important parameter to evaluate the catalytic performance. The long-term durability of the Co@Ir/NC-10% sample was assessed and compared with Pt/C by measuring the polarization curves before and after 3000 cycles between −0.234 and −0.034 V at 100 mV s^{-1}. As illustrated in Figure 5d, the polarization curve of Co@Ir/NC-10% retained almost similar performance with the initial test, with the overpotential just shifted 12 mV negatively. While in contrast, Pt/C exhibited a negative shift of 37 mV under the same conditions, much larger than that of Co@Ir/NC-10%. The results suggest that markedly superior durability than that of Pt/C for Co@Ir/NC-10% was acquired.

In addition to using 1 M KOH as electrolyte for the HER test, the HER catalytic performance was also evaluated in 0.5 M H_2SO_4. Figure S5 presents the LSV polarization curves of the series samples and Pt/C in 0.5 M H_2SO_4 with a scan rate of 10 mV s^{-1}. Pt/C exhibited the best activity as expected, while Co/NC displayed the lowest activity. Similar to 1 M KOH, the HER activity first intensified then diminished with an increasing Ir amount in 0.5 M H_2SO_4. To afford a current density of 10 mA cm^{-2}, the required overpotential was −29.4 mV for Co@

DOI: 10.1021/acssuschemeng.7b04777
ACS Sustainable Chem. Eng. 2018, 6, 5105−5114

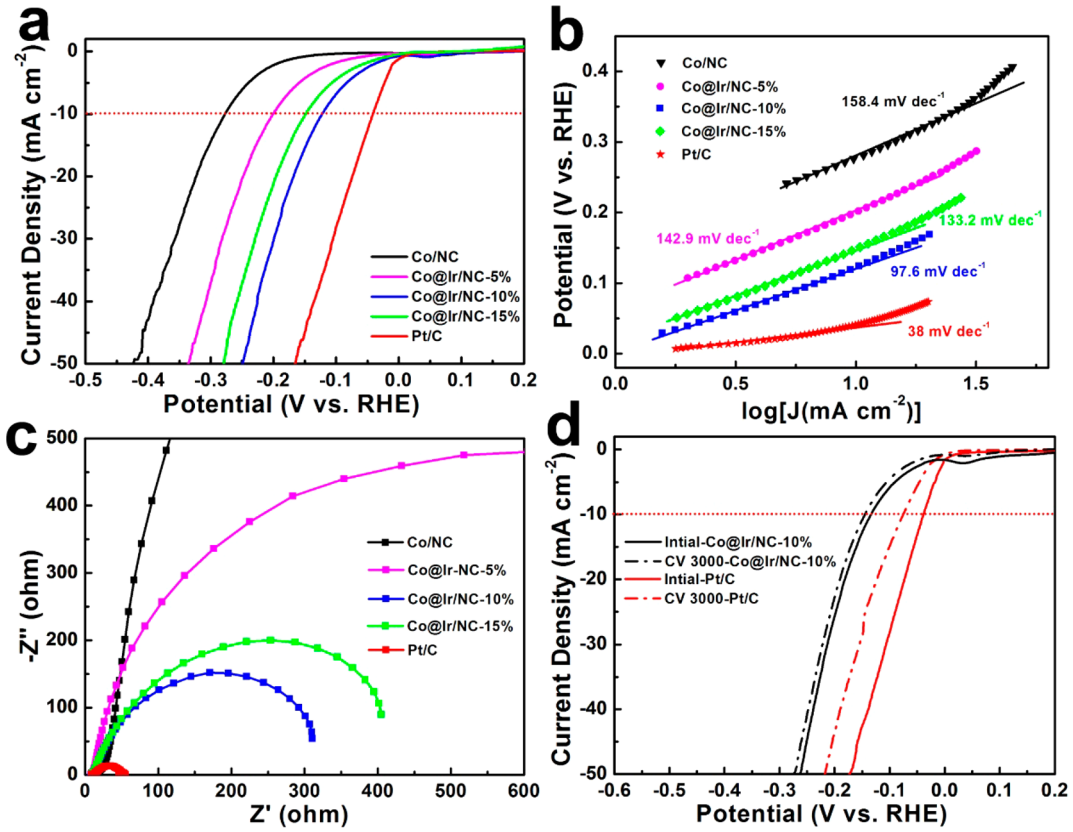

Figure 5. (a) LSV curves of Co/NC, Co@Ir/NC-5%, Co@Ir/NC-10%, Co@Ir/NC-15%, and Pt/C in N_2-saturated 1 M KOH solution at the potential scan rate of 10 mV s^{-1}. (b) Tafel plots of different catalysts in HER derived from the HER polarization curves. (c) Electrochemical impedance spectra of various catalyst samples for HER at −0.07 V versus RHE. (d) HER polarization cures of Co@Ir/NC-10% and Pt/C with the same mass loading and durability test after 3000 cycles in 1 M KOH.

Ir/NC-10%, close to the value of Pt/C (−13.5 mV). As shown in Figure S6, the Tafel slope of different catalysts was then calculated from the Tafel plots. Co/NC exhibited the highest value, and Pt/C demonstrated the lowest value of 33.2 mV dec^{-1}. The Co@Ir/NC-10% sample displayed the lowest Tafel slope (41.9 mV dec^{-1}) among the series, close to that of Pt/C. This confirms that this sample possessed the best electrocatalytic HER activity in acid electrolyte and held a close or comparable activity with Pt/C. Furthermore, to assess its long-term durability, the accelerated durability test was conducted for Co@Ir/NC-10% and Pt/C in 0.5 M H_2SO_4, as shown in Figure S7. After 3000 cycles, at a current density of 10 mA cm^{-2}, the required overpotential shifted negatively ~91.5 mV for Pt/C, while only ~59.7 mV shift was observed for Co@Ir/NC-10%. The results suggest that Co@Ir/NC-10% possessed superior durability than Pt/C for HER in acid electrolyte as well.

It is worth noting that, either the OER or HER performance of the Co@Ir/NC-10% sample is superior, or at least comparable with recently reported Ir based electrocatalysts and other electrocatalysts. The OER comparison results are compiled in Table S2. For instance, by employing 1 M KOH as electrolyte, to afford a current density of 10 mA cm^{-2}, the required overpotential for Ir electrocatalysts was 0.43 V.[17] While in another report, in 1 M NaOH at 10 mA cm^{-2}, the overpotential was 0.32 V for IrO_x catalyst.[49] Under almost similar conditions, such value is much lower for Co@Ir/NC-10% (0.28 V). Table S3 summarizes the HER comparison results. With 0.5 M H_2SO_4 as electrolyte employed, to reach a current density of 10 mA cm^{-2}, the threshold overpotential were 22, 28, 34, and 34 mV for Ru@C_2N,[50] RuCo@NC (1 M HCl as electrolyte),[42] Ni@C,[51] and Mo_2C@NPC/NPRGO,[52] respectively, all of which are close to or comparable with that of Co@Ir/NC-10% (29.4 mV).

To unravel the physical origin of the different electrocatalytic activities of the series samples, the electrochemically active surface area (ECSA) measurements were performed.[53] The cyclic voltammograms acquired in N_2-saturated 0.05 M H_2SO_4 at a scan rate of 50 mV/s can be found in Figure S8. The ECSA value can be calculated by

$$\mathrm{ECSA} = \frac{Q_r}{mC}$$

where Q_r is the hydrogen adsorption charge, m is the Ir mass loading, and C is the charge of full monolayer coverage of H atoms onto clean polycrystalline Ir (218 μC cm^{-2}).[54] The calculated ECSA values were 30.56, 60.00, and 40.89 m^2 g^{-1} for the sample of Co@Ir/NC-5%, Co@Ir/NC-10%, and Co@Ir/NC-15%, respectively. With the increasing of the Ir amount, the ECSA value first increased then decreased, consistent with the electrocatalytic activity change trend. The sample of Co@Ir/NC-10% possessed the largest ECSA value, leading to the best OER and HER performance in the series.

The intriguing excellent electrocatalytic activity toward OER and HER for the sample of Co@Ir/NC might be attributed to the several factors. First of all, the Ir shell can provide various active sites for electrocatalytic reaction especially for OER,[16,19,22,43] while previous investigations have indicated

DOI: 10.1021/acssuschemeng.7b04777
ACS Sustainable Chem. Eng. 2018, 6, 5105−5114

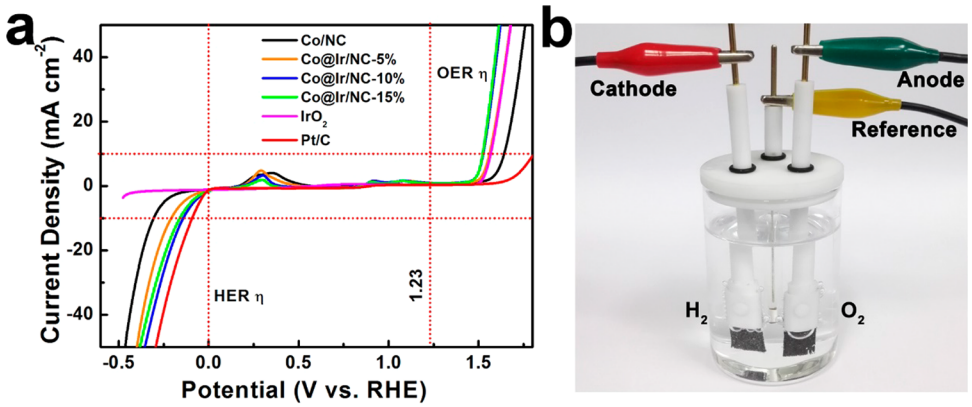

Figure 6. (a) Combined OER and HER catalytic behavior of Co/NC, Co@Ir/NC-5%, Co@Ir/NC-10%, Co@Ir/NC-15%, IrO_2, and Pt/C at a scan rate of 10 mV s^{-1} in 1 M KOH aqueous solution. (b) Optical image of electrocatalytic water electrolysis (generation of H_2 and O_2) through the catalyst of Co@Ir/NC-10% catalyst coated on a carbon fiber paper as anode and cathode in 1 M KOH at an applied potential of 1.7 V vs RHE.

that the Co-NC skeleton is very active for HER electrocatalysis.[13,55] Second, the synergistic effects between the Co core and the Ir shell probably facilitated the electron transfer kinetics during the reaction process, as manifested by the electron transfer behaviors detected in XPS measurements.[25,26] Lastly, rather than serving as a support, the nitrogen doped porous carbon actually played a critical role in metal−carbon interaction,[56−58] which can significantly boost the electrocatalytic performance.

Furthermore, to achieve a better understanding of the series of samples as bifunctional catalyst toward OER and HER, the combined HER and OER behaviors of the series of samples were examined and compared with both IrO_2 and Pt/C. As illustrated in Figure 6a, the left part is the HER process, and the equilibrium potential (U^o) is 0 V vs RHE. IrO_2 exhibited negligible HER activity, and to afford a current density of 10 mA cm^{-2}, the required overpotential was −0.145 V for Co@Ir/NC-10%, most close to that of Pt/C. The right part is the OER process, and the equilibrium potential (U^o) is 1.23 V vs RHE.[59] Pt/C displayed barely OER activity, and to reach a current density of 10 mA cm^{-2}, the smallest overpotential required was 292 mV for the Co@Ir/NC-10% sample, lower than that of benchmark IrO_2 catalyst (335 mV).

Inspired by the excellent OER and HER catalytic performance of the sample of Co@Ir/NC-10%, a two-electrode electrolyzer using Co@Ir/NC-10% was assembled to evaluate its performance for practical overall water splitting in 1 M KOH. As shown in Figure 6b, with an applied potential of 1.7 V vs RHE, appreciable gas bubbles on the electrode surface of cathode and anode can be observed, respectively. It is also interesting to note that the evolution of H_2 at the anode is much faster than that of O_2 at the cathode. This is probably due to the much higher solubility of O_2 in water than H_2 as well as lower reaction kinetics of O_2 formation caused by multiple electron transfer.[60]

CONCLUSIONS

In conclusion, Co@Ir core−shell nanoparticles encapsulated in nitrogen-doped porous carbon derived from ZIF-67 were fabricated by a facile approach for overall water splitting in this study. Among a series of samples, Co@Ir/NC-10% exhibited the best catalytic performance, with OER activity superior than IrO_2, and HER activity close to Pt/C. Moreover, markedly higher long-term stability than IrO_2 for OER and superior long-term durability than Pt/C for HER were also obtained for Co@Ir/NC-10%. Finally, the overall water splitting catalyzed by the series of composites was explored and visually observed. Our results showed a new way to design and prepare highly efficient and durable bifunctional electrocatalyst for overall water splitting with low noble metal loading, which are of broad fundamental interest and great potential application values.[61,62]

ASSOCIATED CONTENT

Supporting Information

The Supporting Information is available free of charge on the ACS Publications website at DOI: 10.1021/acssuschemeng.7b04777.

Additional tables, SEM images, nitrogen adsorption/desorption isotherms, HR-TEM images, XPS survey scan spectra, additional polarization curves, Tafel plots, durability tests, and cyclic voltammograms (PDF)

AUTHOR INFORMATION

Corresponding Authors

*E-mail: x_f_wang@163.com (X.W.).
*E-mail: zhht@scut.edu.cn (Z.T.).

ORCID

Zhenghua Tang: 0000-0003-0718-3164
Shaowei Chen: 0000-0002-3668-8551
Xiufang Wang: 0000-0003-0822-2890

Notes

The authors declare no competing financial interest.

ACKNOWLEDGMENTS

We acknowledge financial support from the National Natural Science Foundation of China (No. 21501059 for Z.H.T. and No. 21373061 for X.F.W), Guangdong Natural Science Funds for Distinguished Young Scholars (No. 2015A030306006), Project of Public Interest Research and Capacity Building of Guangdong Province (2015A010105009), Science and Technology Program of Guangdong Province (No. 2017A050506014), and Guangdong Innovative and Entrepreneurial Research Team Program (No. 2014ZT05N200).

DOI: 10.1021/acssuschemeng.7b04777
ACS Sustainable Chem. Eng. 2018, 6, 5105−5114

REFERENCES

(1) Jiang, Q.; Zeng, X.; Wang, N.; Xiao, Z.; Guo, Z.; Lu, J. Electrochemical Lithium Doping Induced Property Changes In Halide Perovskite CsPbBr3 Crystal. *ACS Energy Lett.* **2018**, *3*, 264−269.

(2) Zhang, L.; Qin, M.; Yu, W.; Zhang, Q.; Xie, H.; Sun, Z.; Shao, Q.; Guo, X.; Hao, L.; Zheng, Y.; Guo, Z. Heterostructured TiO2/WO3 Nanocomposites for Photocatalytic Degradation of Toluene under Visible Light. *J. Electrochem. Soc.* **2017**, *164*, H1086−H1090.

(3) Zhang, L.; Yu, W.; Han, C.; Guo, J.; Zhang, Q.; Xie, H.; Shao, Q.; Sun, Z.; Guo, Z. Large Scaled Synthesis of Heterostructured Electrospun TiO2/SnO2 Nanofibers with an Enhanced Photocatalytic Activity. *J. Electrochem. Soc.* **2017**, *164*, H651−H656.

(4) Huang, J.; Cao, Y.; Shao, Q.; Peng, X.; Guo, Z. Magnetic Nanocarbon Adsorbents with Enhanced Hexavalent Chromium Removal: Morphology Dependence of Fibrillar vs Particulate Structures. *Ind. Eng. Chem. Res.* **2017**, *56*, 10689−10701.

(5) Song, B.; Wang, T.; Sun, H.; Shao, Q.; Zhao, J.; Song, K.; Hao, L.; Wang, L.; Guo, Z. Two-step hydrothermally synthesized carbon nanodots/WO3 photocatalysts with enhanced photocatalytic performance. *Dalton Transac.* **2017**, *46*, 15769−15777.

(6) Lin, C.; Hu, L.; Cheng, C.; Sun, K.; Guo, X.; Shao, Q.; Li, J.; Wang, N.; Guo, Z. Nano-TiNb2O7/carbon nanotubes composite anode for enhanced lithium-ion storage. *Electrochim. Acta* **2018**, *260*, 65−72.

(7) Zou, X.; Zhang, Y. Noble metal-free hydrogen evolution catalysts for water splitting. *Chem. Soc. Rev.* **2015**, *44*, 5148−5180.

(8) Wang, J.; Xu, F.; Jin, H.; Chen, Y.; Wang, Y. Non-Noble Metal-based Carbon Composites in Hydrogen Evolution Reaction: Fundamentals to Applications. *Adv. Mater.* **2017**, *29*, 1605838.

(9) Luo, J.; Im, J.-H.; Mayer, M. T.; Schreier, M.; Nazeeruddin, M. K.; Park, N.-G.; Tilley, S. D.; Fan, H. J.; Grätzel, M. Water photolysis at 12.3% efficiency via perovskite photovoltaics and Earth-abundant catalysts. *Science* **2014**, *345*, 1593.

(10) Walter, M. G.; Warren, E. L.; McKone, J. R.; Boettcher, S. W.; Mi, Q.; Santori, E. A.; Lewis, N. S. Solar Water Splitting Cells. *Chem. Rev.* **2010**, *110*, 6446−6473.

(11) Wang, M.; Chen, L.; Sun, L. Recent progress in electrochemical hydrogen production with earth-abundant metal complexes as catalysts. *Energy Environ. Sci.* **2012**, *5*, 6763−6778.

(12) Liu, J.; Liu, Y.; Liu, N.; Han, Y.; Zhang, X.; Huang, H.; Lifshitz, Y.; Lee, S.-T.; Zhong, J.; Kang, Z. Metal-free efficient photocatalyst for stable visible water splitting via a two-electron pathway. *Science* **2015**, *347*, 970.

(13) Wang, J.; Cui, W.; Liu, Q.; Xing, Z.; Asiri, A. M.; Sun, X. Recent Progress in Cobalt-Based Heterogeneous Catalysts for Electrochemical Water Splitting. *Adv. Mater.* **2016**, *28*, 215−230.

(14) Suntivich, J.; May, K. J.; Gasteiger, H. A.; Goodenough, J. B.; Shao-Horn, Y. A Perovskite Oxide Optimized for Oxygen Evolution Catalysis from Molecular Orbital Principles. *Science* **2011**, *334*, 1383.

(15) Kanan, M. W.; Nocera, D. G. In Situ Formation of an Oxygen-Evolving Catalyst in Neutral Water Containing Phosphate and Co^{2+}. *Science* **2008**, *321*, 1072.

(16) Özer, E.; Spöri, C.; Reier, T.; Strasser, P. Iridium(1 1 1), Iridium(1 1 0), and Ruthenium(0 0 0 1) Single Crystals as Model Catalysts for the Oxygen Evolution Reaction: Insights into the Electrochemical Oxide Formation and Electrocatalytic Activity. *ChemCatChem* **2017**, *9*, 597−603.

(17) McCrory, C. C. L.; Jung, S.; Ferrer, I. M.; Chatman, S. M.; Peters, J. C.; Jaramillo, T. F. Benchmarking Hydrogen Evolving Reaction and Oxygen Evolving Reaction Electrocatalysts for Solar Water Splitting Devices. *J. Am. Chem. Soc.* **2015**, *137*, 4347−4357.

(18) Rausch, B.; Symes, M. D.; Chisholm, G.; Cronin, L. Decoupled catalytic hydrogen evolution from a molecular metal oxide redox mediator in water splitting. *Science* **2014**, *345*, 1326.

(19) Lettenmeier, P.; Wang, L.; Golla-Schindler, U.; Gazdzicki, P.; Cañas, N. A.; Handl, M.; Hiesgen, R.; Hosseiny, S. S.; Gago, A. S.; Friedrich, K. A. Nanosized IrOx−Ir Catalyst with Relevant Activity for Anodes of Proton Exchange Membrane Electrolysis Produced by a Cost-Effective Procedure. *Angew. Chem., Int. Ed.* **2016**, *55*, 742−746.

(20) Reier, T.; Oezaslan, M.; Strasser, P. Electrocatalytic Oxygen Evolution Reaction (OER) on Ru, Ir, and Pt Catalysts: A Comparative Study of Nanoparticles and Bulk Materials. *ACS Catal.* **2012**, *2*, 1765−1772.

(21) Nong, H. N.; Oh, H.-S.; Reier, T.; Willinger, E.; Willinger, M.-G.; Petkov, V.; Teschner, D.; Strasser, P. Oxide-Supported IrNiOx Core−Shell Particles as Efficient, Cost-Effective, and Stable Catalysts for Electrochemical Water Splitting. *Angew. Chem., Int. Ed.* **2015**, *54*, 2975−2979.

(22) Nong, H. N.; Gan, L.; Willinger, E.; Teschner, D.; Strasser, P. IrOx core-shell nanocatalysts for cost- and energy-efficient electrochemical water splitting. *Chem. Sci.* **2014**, *5*, 2955−2963.

(23) Hu, W.; Zhong, H.; Liang, W.; Chen, S. Ir-Surface Enriched Porous Ir−Co Oxide Hierarchical Architecture for High Performance Water Oxidation in Acidic Media. *ACS Appl. Mater. Interfaces* **2014**, *6*, 12729−12736.

(24) Wang, C.; Sui, Y.; Xiao, G.; Yang, X.; Wei, Y.; Zou, G.; Zou, B. Synthesis of Cu-Ir nanocages with enhanced electrocatalytic activity for the oxygen evolution reaction. *J. Mater. Chem. A* **2015**, *3*, 19669−19673.

(25) Pi, Y.; Shao, Q.; Wang, P.; Guo, J.; Huang, X. General Formation of Monodisperse IrM (M = Ni, Co, Fe) Bimetallic Nanoclusters as Bifunctional Electrocatalysts for Acidic Overall Water Splitting. *Adv. Funct. Mater.* **2017**, *27*, 1700886.

(26) Pei, J.; Mao, J.; Liang, X.; Chen, C.; Peng, Q.; Wang, D.; Li, Y. Ir-Cu nanoframes: one-pot synthesis and efficient electrocatalysts for oxygen evolution reaction. *Chem. Commun.* **2016**, *52*, 3793−3796.

(27) Reier, T.; Pawolek, Z.; Cherevko, S.; Bruns, M.; Jones, T.; Teschner, D.; Selve, S.; Bergmann, A.; Nong, H. N.; Schlögl, R.; Mayrhofer, K. J. J.; Strasser, P. Molecular Insight in Structure and Activity of Highly Efficient, Low-Ir Ir−Ni Oxide Catalysts for Electrochemical Water Splitting (OER). *J. Am. Chem. Soc.* **2015**, *137*, 13031−13040.

(28) Thomsen, J. M.; Sheehan, S. W.; Hashmi, S. M.; Campos, J.; Hintermair, U.; Crabtree, R. H.; Brudvig, G. W. Electrochemical Activation of Cp* Iridium Complexes for Electrode-Driven Water-Oxidation Catalysis. *J. Am. Chem. Soc.* **2014**, *136*, 13826−13834.

(29) Diaz-Morales, O.; Hersbach, T. J. P.; Hetterscheid, D. G. H.; Reek, J. N. H.; Koper, M. T. M. Electrochemical and Spectroelectrochemical Characterization of an Iridium-Based Molecular Catalyst for Water Splitting: Turnover Frequencies, Stability, and Electrolyte Effects. *J. Am. Chem. Soc.* **2014**, *136*, 10432−10439.

(30) Liu, T.; Yu, K.; Gao, L.; Chen, H.; Wang, N.; Hao, L.; Li, T.; He, H.; Guo, Z. A graphene quantum dot decorated SrRuO3 mesoporous film as an efficient counter electrode for high-performance dye-sensitized solar cells. *J. Mater. Chem. A* **2017**, *5*, 17848−17855.

(31) Luo, Q.; Ma, H.; Hao, F.; Hou, Q.; Ren, J.; Wu, L.; Yao, Z.; Zhou, Y.; Wang, N.; Jiang, K.; Lin, H.; Guo, Z. Carbon Nanotube Based Inverted Flexible Perovskite Solar Cells with All-Inorganic Charge Contacts. *Adv. Funct. Mater.* **2017**, *27*, 1703068.

(32) Cheng, C.; Fan, R.; Wang, Z.; Shao, Q.; Guo, X.; Xie, P.; Yin, Y.; Zhang, Y.; An, L.; Lei, Y.; Ryu, J. E.; Shankar, A.; Guo, Z. Tunable and weakly negative permittivity in carbon/silicon nitride composites with different carbonizing temperatures. *Carbon* **2017**, *125*, 103−112.

(33) You, B.; Jiang, N.; Sheng, M.; Drisdell, W. S.; Yano, J.; Sun, Y. Bimetal−Organic Framework Self-Adjusted Synthesis of Support-Free Nonprecious Electrocatalysts for Efficient Oxygen Reduction. *ACS Catal.* **2015**, *5*, 7068−7076.

(34) Wang, L.; Tang, Z.; Yan, W.; Wang, Q.; Yang, H.; Chen, S. Co@Pt Core@Shell nanoparticles encapsulated in porous carbon derived from zeolitic imidazolate framework 67 for oxygen electroreduction in alkaline media. *J. Power Sources* **2017**, *343*, 458−466.

(35) Shen, K.; Chen, L.; Long, J.; Zhong, W.; Li, Y. MOFs-Templated Co@Pd Core−Shell NPs Embedded in N-Doped Carbon Matrix with Superior Hydrogenation Activities. *ACS Catal.* **2015**, *5*, 5264−5271.

(36) Shen, K.; Qian, W.; Wang, N.; Su, C.; Wei, F. Fabrication of c-Axis Oriented ZSM-5 Hollow Fibers Based on an in Situ Solid−Solid

DOI: 10.1021/acssuschemeng.7b04777
ACS Sustainable Chem. Eng. 2018, 6, 5105−5114

Transformation Mechanism. *J. Am. Chem. Soc.* **2013**, *135*, 15322−15325.
(37) Chen, Y.; Jie, S.; Yang, C.; Liu, Z. Active and efficient Co-N/C catalysts derived from cobalt porphyrin for selective oxidation of alkylaromatics. *Appl. Surf. Sci.* **2017**, *419*, 98−106.
(38) Ding, W.; Wei, Z.; Chen, S.; Qi, X.; Yang, T.; Hu, J.; Wang, D.; Wan, L.-J.; Alvi, S. F.; Li, L. Space-Confinement-Induced Synthesis of Pyridinic- and Pyrrolic-Nitrogen-Doped Graphene for the Catalysis of Oxygen Reduction. *Angew. Chem., Int. Ed.* **2013**, *52*, 11755−11759.
(39) Wang, N.; Li, L.; Zhao, D.; Kang, X.; Tang, Z.; Chen, S. Graphene Composites with Cobalt Sulfide: Efficient Trifunctional Electrocatalysts for Oxygen Reversible Catalysis and Hydrogen Production in the Same Electrolyte. *Small* **2017**, *13*, 1701025.
(40) Jin, H.; Wang, J.; Su, D.; Wei, Z.; Pang, Z.; Wang, Y. In situ Cobalt−Cobalt Oxide/N-Doped Carbon Hybrids As Superior Bifunctional Electrocatalysts for Hydrogen and Oxygen Evolution. *J. Am. Chem. Soc.* **2015**, *137*, 2688−2694.
(41) Ganesan, P.; Prabu, M.; Sanetuntikul, J.; Shanmugam, S. Cobalt Sulfide Nanoparticles Grown on Nitrogen and Sulfur Codoped Graphene Oxide: An Efficient Electrocatalyst for Oxygen Reduction and Evolution Reactions. *ACS Catal.* **2015**, *5*, 3625−3637.
(42) Su, J.; Yang, Y.; Xia, G.; Chen, J.; Jiang, P.; Chen, Q. Ruthenium-cobalt nanoalloys encapsulated in nitrogen-doped graphene as active electrocatalysts for producing hydrogen in alkaline media. *Nat. Commun.* **2017**, *8*, 14969.
(43) Yuan, L.; Yan, Z.; Jiang, L.; Wang, E.; Wang, S.; Sun, G. Gold-iridium bifunctional electrocatalyst for oxygen reduction and oxygen evolution reactions. *J. Energy Chem.* **2016**, *25*, 805−810.
(44) Sui, S.; Ma, L.; Zhai, Y. TiC supported Pt−Ir electrocatalyst prepared by a plasma process for the oxygen electrode in unitized regenerative fuel cells. *J. Power Sources* **2011**, *196*, 5416−5422.
(45) Atanasoski, R. T.; Atanasoska, L. L.; Cullen, D. A.; Haugen, G. M.; More, K. L.; Vernstrom, G. D. Fuel Cells Catalyst for Start-Up and Shutdown Conditions: Electrochemical, XPS, and STEM Evaluation of Sputter-Deposited Ru, Ir, and Ti on Pt-Coated Nanostructured Thin Film Supports. *Electrocatalysis* **2012**, *3*, 284−297.
(46) Chen, J. S.; Ren, J.; Shalom, M.; Fellinger, T.; Antonietti, M. Stainless Steel Mesh-Supported NiS Nanosheet Array as Highly Efficient Catalyst for Oxygen Evolution Reaction. *ACS Appl. Mater. Interfaces* **2016**, *8*, 5509−5516.
(47) Ha, D.-H.; Han, B.; Risch, M.; Giordano, L.; Yao, K. P. C.; Karayaylali, P.; Shao-Horn, Y. Activity and stability of cobalt phosphides for hydrogen evolution upon water splitting. *Nano Energy* **2016**, *29*, 37−45.
(48) Liu, T.; Ma, X.; Liu, D.; Hao, S.; Du, G.; Ma, Y.; Asiri, A. M.; Sun, X.; Chen, L. Mn Doping of CoP Nanosheets Array: An Efficient Electrocatalyst for Hydrogen Evolution Reaction with Enhanced Activity at All pH Values. *ACS Catal.* **2017**, *7*, 98−102.
(49) McCrory, C. C. L.; Jung, S.; Peters, J. C.; Jaramillo, T. F. Benchmarking Heterogeneous Electrocatalysts for the Oxygen Evolution Reaction. *J. Am. Chem. Soc.* **2013**, *135*, 16977−16987.
(50) Mahmood, J.; Li, F.; Jung, S.-M.; Okyay, M. S.; Ahmad, I.; Kim, S.-J.; Park, N.; Jeong, H. Y.; Baek, J.-B. An efficient and pH-universal ruthenium-based catalyst for the hydrogen evolution reaction. *Nat. Nanotechnol.* **2017**, *12*, 441−446.
(51) Fan, L.; Liu, P. F.; Yan, X.; Gu, L.; Yang, Z. Z.; Yang, H. G.; Qiu, S.; Yao, X. Atomically isolated nickel species anchored on graphitized carbon for efficient hydrogen evolution electrocatalysis. *Nat. Commun.* **2016**, *7*, 10667.
(52) Li, J.-S.; Wang, Y.; Liu, C.-H.; Li, S.-L.; Wang, Y.-G.; Dong, L.-Z.; Dai, Z.-H.; Li, Y.-F.; Lan, Y.-Q. Coupled molybdenum carbide and reduced graphene oxide electrocatalysts for efficient hydrogen evolution. *Nat. Commun.* **2016**, *7*, 11204.
(53) Zheng, J.; Zhuang, Z.; Xu, B.; Yan, Y. Correlating Hydrogen Oxidation/Evolution Reaction Activity with the Minority Weak Hydrogen-Binding Sites on Ir/C Catalysts. *ACS Catal.* **2015**, *5*, 4449−4455.
(54) Zhao, S.; Yu, H.; Maric, R.; Danilovic, N.; Capuano, C. B.; Ayers, K. E.; Mustain, W. E. Calculating the Electrochemically Active Surface Area of Iridium Oxide in Operating Proton Exchange Membrane Electrolyzers. *J. Electrochem. Soc.* **2015**, *162*, F1292−F1298.
(55) Zou, X.; Huang, X.; Goswami, A.; Silva, R.; Sathe, B. R.; Mikmeková, E.; Asefa, T. Cobalt-Embedded Nitrogen-Rich Carbon Nanotubes Efficiently Catalyze Hydrogen Evolution Reaction at All pH Values. *Angew. Chem., Int. Ed.* **2014**, *53*, 4372−4376.
(56) Li, R.; Wei, Z.; Gou, X. Nitrogen and Phosphorus Dual-Doped Graphene/Carbon Nanosheets as Bifunctional Electrocatalysts for Oxygen Reduction and Evolution. *ACS Catal.* **2015**, *5*, 4133−4142.
(57) Niu, W.; Li, L.; Liu, X.; Wang, N.; Liu, J.; Zhou, W.; Tang, Z.; Chen, S. Mesoporous N-Doped Carbons Prepared with Thermally Removable Nanoparticle Templates: An Efficient Electrocatalyst for Oxygen Reduction Reaction. *J. Am. Chem. Soc.* **2015**, *137*, 5555−5562.
(58) Kuang, M.; Wang, Q.; Han, P.; Zheng, G. Cu, Co-Embedded N-Enriched Mesoporous Carbon for Efficient Oxygen Reduction and Hydrogen Evolution Reactions. *Adv. Energy Mater.* **2017**, *7*, 1700193.
(59) Jiao, Y.; Zheng, Y.; Jaroniec, M.; Qiao, S. Z. Design of Electrocatalysts for Oxygen- and Hydrogen-Involving Energy Conversion Reactions. *Chem. Soc. Rev.* **2015**, *44*, 2060−2086.
(60) Maruthapandian, V.; Mathankumar, M.; Saraswathy, V.; Subramanian, B.; Muralidharan, S. Study of the Oxygen Evolution Reaction Catalytic Behavior of $Co_xNi_{1-x}Fe_2O_4$ in Alkaline Medium. *ACS Appl. Mater. Interfaces* **2017**, *9*, 13132−13141.
(61) Li, Y.; Zhou, B.; Zheng, G.; Liu, X.; Li, T.; Yan, C.; Cheng, C.; Dai, K.; Liu, C.; Shen, C.; Guo, Z. Continuously prepared highly conductive and stretchable SWNT/MWNT synergistically composited electrospun thermoplastic polyurethane yarns for wearable sensing. *J. Mater. Chem. C* **2018**, *6*, 2258.
(62) Guan, X.; Zheng, G.; Dai, K.; Liu, C.; Yan, X.; Shen, C.; Guo, Z. Carbon Nanotubes-Adsorbed Electrospun PA66 Nanofiber Bundles with Improved Conductivity and Robust Flexibility. *ACS Appl. Mater. Interfaces* **2016**, *8*, 14150−14159.

DOI: 10.1021/acssuschemeng.7b04777
ACS Sustainable Chem. Eng. 2018, 6, 5105−5114